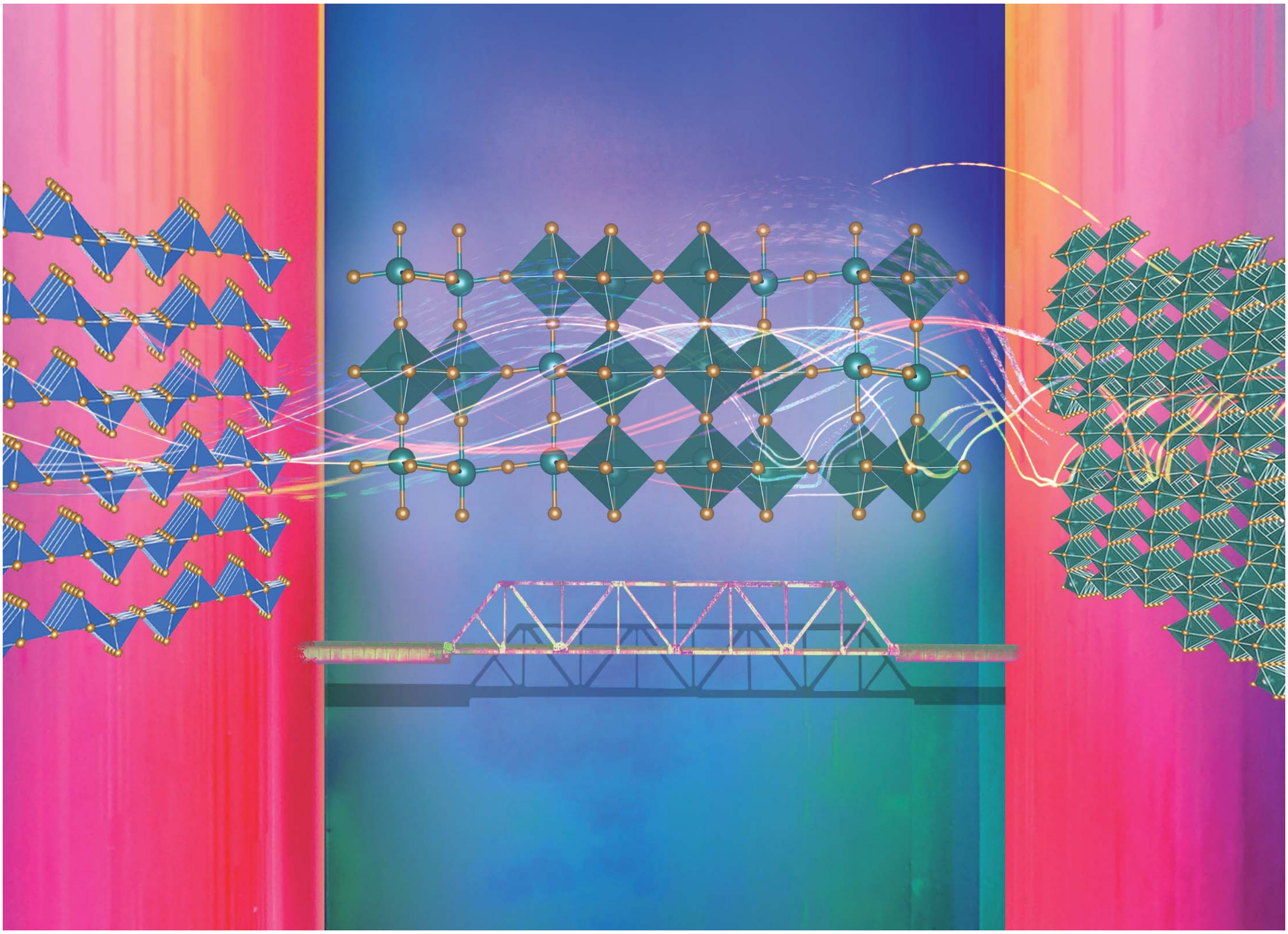

Highlighting a study on the battery cycling and atomic structure stability of the metastable '*R*' polymorph of Nb_2O_5 from Professor Megan M. Butala's laboratory in the Department of Materials Science and Engineering at the University of Florida (United States).

R-Nb_2O_5 has an 'idealized' V_2O_5 structure and Wadsley–Roth-like structural stability during Li-ion battery cycling

With Wadsley-Roth-like 'slabs' and an 'idealized' V_2O_5 structure, metastable *R*–Nb_2O_5 bridges two well-studied families of Li-ion battery electrodes. Inter- and intra-polyhedral connectivity stabilize the structure against polyhedral rotations during lithiation and delithiation, providing excellent reversibility with negligible structure changes during cycling.

As featured in:

See Megan M. Butala *et al.*,
J. Mater. Chem. A, 2023, **11**, 5559.

ROYAL SOCIETY
OF CHEMISTRY

rsc.li/materials-a

Registered charity number: 207890

Journal of
Materials Chemistry A

PAPER

View Article Online
View Journal | View Issue

Cite this: *J. Mater. Chem. A*, 2023, **11**, 5559

Received 4th November 2022
Accepted 20th January 2023

DOI: 10.1039/d2ta08653k

rsc.li/materials-a

R-Nb_2O_5 has an 'idealized' V_2O_5 structure and Wadsley–Roth-like structural stability during Li-ion battery cycling†

Kausturi Parui, Alexander D. Lee, Shornam Gandhi and Megan M. Butala*

The adoption of batteries across diverse applications requires electrode materials with a wider range of performance metrics, such as cost, safety, and material availability. Along the path to discovering new commercially viable materials, a fundamental understanding of chemical and atomic structure features that provide structural stability and effective ion transport is essential. In support of new understanding, we report the cycling behavior of metastable *R*-Nb_2O_5. *R*-Nb_2O_5 adopts an 'idealized' V_2O_5 structure, in which $[NbO_6]$ octahedra alternate in edge- and corner-sharing resulting in ReO_3-like slabs, whereas Wadsley–Roth materials have ReO_3-like blocks, linked through edge-sharing octahedra at intersecting crystallographic shear planes. We find that this slab structure is stable during cycling, with minor atomic structure changes and cycling curves that are symmetric on discharge and charge, resembling the behavior of Wadsley–Roth materials more than other related materials, such as ReO_3, V_2O_5, or Nb_3O_7F. Based on our findings, *R*-Nb_2O_5 can serve as a 'structural bridge' between Wadsley–Roth block structures and V_2O_5, through which we can relate inter- and intra-polyhedral structures to cycling behavior and structural stability during cycling.

1 Introduction

Early transition metal oxides featuring crystallographic shear planes are a technologically and fundamentally compelling family of Li-ion battery electrode candidates. These materials, sometimes referred to as Wadsley–Roth or Magnéli phases,[1–5] have demonstrated excellent performance as high potential anodes. With operating potentials between 1 V and 1.5 V and excellent rate capabilities, they offer a pathway to safe, high-power Li-ion batteries as alternatives to graphite and $Li_4Ti_5O_{12}$.[6–8] Wadsley–Roth (WR) materials can also have multi-electron redox, in which more than one redox reaction occurs per redox active transition metal, contributing to high energy densities, *e.g.*, reduction of Nb^{5+} to Nb^{3+}, allowing for storage of >1 mol Li per transition metal, M.[5,9–12]

In addition to being technologically relevant, WR materials provide a foundation for identifying atomic and electronic structure features that support effective transport of ions and electrons.[9,13,14] WR materials have ReO_3-like blocks, in which $[MO_6]$ octahedra are corner-sharing (Fig. 1a and c) with square channels that provide fast Li transport. These blocks are connected across crystallographic shear planes, at which $[MO_6]$ octahedra are edge-sharing (Fig. 1b and c). During lithiation of ReO_3, $[ReO_6]$ octahedra rotate around corner-sharing vertices.[4,15] In contrast, in WR materials, the edge-sharing octahedra at crystallographic shear planes stabilize against this rotation, keeping square channels accessible for fast Li^+ transport.[9,11] In addition to structural stability, edge-sharing octahedra have a favorable overlap of d-electron orbitals, which results in high electronic conductivity upon even minor reduction, contributing to their high-rate capabilities.[11,16,17]

Among WR and related materials studied as battery electrodes, there are many niobates,[16,18] including those with the chemical formula Nb_2O_5.[17,19–24] We report here, for the first time, the cycling behavior and charge storage mechanism of yet another polymorph *R*-Nb_2O_5. '*R*' represents a "neutral designation",[19,25,26] and is not related to the crystal system or preparation conditions. This metastable polymorph adopts an idealized V_2O_5 structure (Fig. 1f and 2)[2] and was first identified by Gruehn.[25] *R*-Nb_2O_5 can be described relative to WR block structures as having ReO_3-like slabs (rather than blocks) connected by parallel (rather than perpendicular) shear planes (Fig. 2a).[2,27]

WR block structures can be described by the connectivity of $[MO_6]$ octahedra, specifically in terms of the number of corner-sharing octahedra in a given direction. For example, a block that is *m* corner-sharing octahedra wide, *n* high, and infinite in the third direction would be represented as $(m \times n)\infty$.[3] For *H*-Nb_2O_5, this representation would be $(3 \times 5)_\infty$ (Fig. 1c).

Department of Materials Science and Engineering, University of Florida, Gainesville, FL 32611, USA. E-mail: mbutala@ufl.edu

† Electronic supplementary information (ESI) available: Additional details and results from Rietveld refinements of atomic structure models as well as cycling data in Swagelok cells, representative of cycling from which *ex situ* discharged and charged powders were prepared, and coin cells cycled at C/10 and 1C. See DOI: **https://doi.org/10.1039/d2ta08653k**

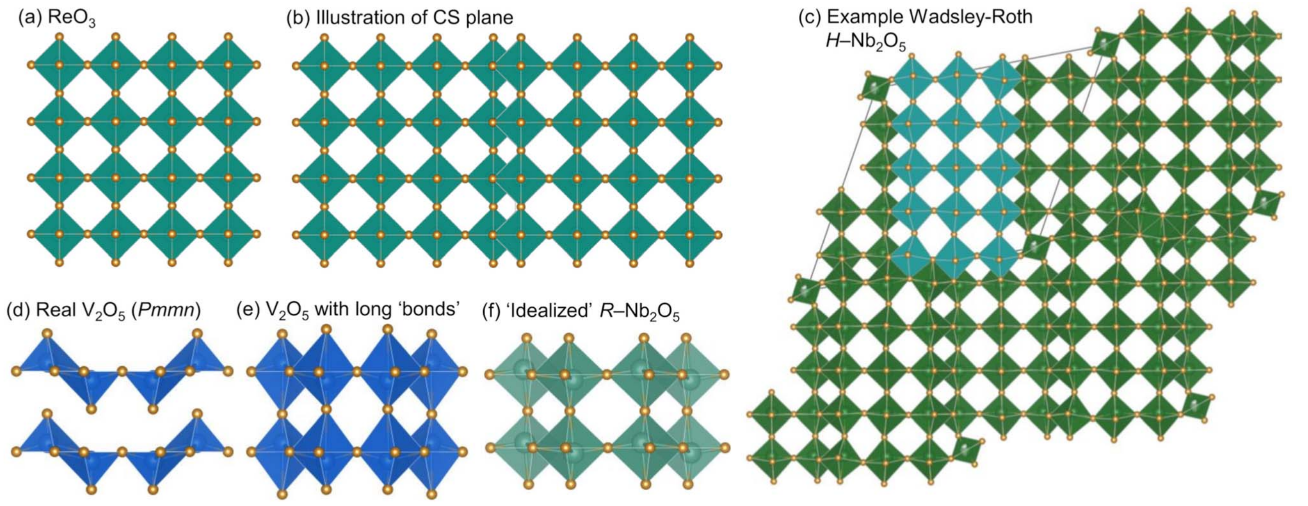

Fig. 1 (a) ReO_3 has only corner-sharing $[MO_6]$ octahedra. (b) Adjacent ReO_3-like blocks offset by $\frac{1}{2}$ an octahedron in 2 directions make a crystallographic shear (CS) plane with edge-sharing $[MO_6]$ octahedra. (c) Wadsley–Roth structures are comprised of ReO_3-like blocks connected by intersecting CS planes; *H*-Nb_2O_5 is shown as an example. (d) V_2O_5 has layers of edge- and corner-sharing $[VO_5]$ square pyramids. (e) Connecting the long V–O distance across the layers, a relationship between (d) real and (f) 'idealized' V_2O_5 structures can be visualized. (f) Metastable polymorph *R*-Nb_2O_5 adopts an idealized V_2O_5 structure with edge- and corner-sharing octahedra.

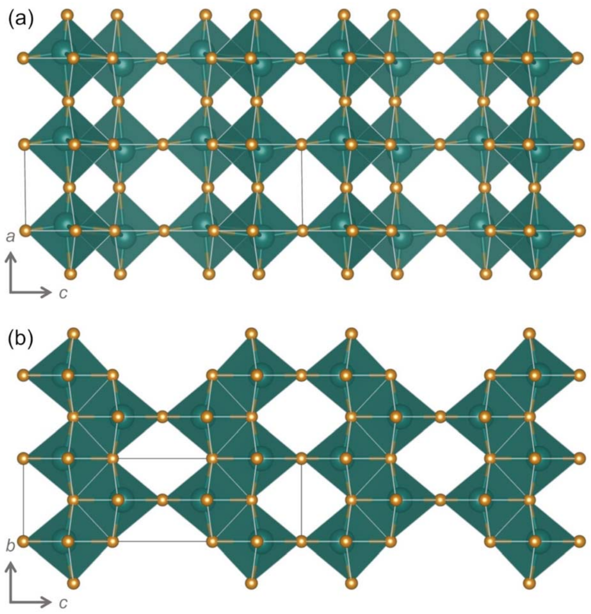

Fig. 2 Visualizations of *R*-Nb_2O_5 based on the original report (ICSD collection code 25765)[25] viewed along the (a) [010] and (b) [100] directions.

Borrowing the WR structure notation,[3] the structure of *R*-Nb_2O_5 can be represented as $(2 \times \infty)_\infty$.

Both α-V_2O_5 and ReO_3 can be considered as 'parent structures' for *R*-Nb_2O_5.[27,28] Like ReO_3, V_2O_5 also undergoes polyhedral rotations during lithiation that result in extensive atomic structure changes.[29,30] V_2O_5 has layers composed of edge- and corner-sharing $[VO_5]$ square pyramids (Fig. 1d). Across the layers, there is a long V–O distance (≈ 2.8 Å); when a 'bond' is drawn between these atoms, V_2O_5 can be visualized as a three-dimensionally-connected structure (Fig. 1e). The larger ionic radius of Nb relative to that of V results in the octahedral, rather than square-pyramidal, coordination of Nb in *R*-Nb_2O_5, approaching a relatively idealized structure.[2,31] Given the different atomic structure evolutions and stabilizations of ReO_3 and WR block structures, we analogously find that *R*-Nb_2O_5 has improved structural stability upon lithiation relative to V_2O_5. In addition to being stable against polyhedral rotation during lithiation, we also find that *R*-Nb_2O_5 has minimal atomic structure evolution during cycling, akin to the relatively small changes in WR materials, for example, unit cell volume changes $\leq 6\%$.[10,11]

The 'ideality' of *R*-Nb_2O_5 relative to that of α-V_2O_5 can be illustrated by comparing their distributions of M–O distances. For *R*-Nb_2O_5, they range from 1.7 Å to 2.3 Å (this work); this is narrower than the range for V_2O_5, which is from 1.58 Å to 2.8 Å,[32] and broader than that for ReO_3, in which there is a single Re–O bond length of 1.9 Å.[33] Nb_3O_7F is another slab structure, denoted as $(3 \times \infty)_\infty$, that has also been studied as a Li-ion electrode[15] and has a similar distribution as *R*-Nb_2O_5, from 1.85 Å to 2.2 Å.[34]

Overall, we find that the cycling behavior and structural stability of *R*-Nb_2O_5 are more similar to WRs than to ReO_3,[4,35] α-V_2O_5,[29] or Nb_3O_7F.[15] *R*-Nb_2O_5 has symmetric discharge and charge profiles that do not significantly change between the first and later cycles. In addition, atomic structure changes are minimal, with no evidence of the polyhedral rotation that ReO_3 or V_2O_5 undergo during lithiation. We observed unit cell changes of less than 5% and a reduced off-centering of Nb in cycled products.[9–11]

2 Results and discussion

2.1 Synthesis and characterization of *R*-Nb_2O_5

The *R* polymorph of Nb_2O_5 was prepared through soft chemical methods, specifically, through the drying and decomposition of hydrated precursor $H_3ONb_3O_8$.[36] $H_3ONb_3O_8$ was produced from KNb_3O_8, a layered niobate, through ion-exchange in nitric acid.[36–38] KNb_3O_8 was prepared using molten salt synthesis in an excess of KCl, which facilitates the mass transport among precursors to form a phase pure product.[18,39]

Bragg peak positions of the prepared *R*-Nb_2O_5 are consistent with the structure originally reported by Gruehn,[25] which is evident in neutron diffraction data (POWGEN at Oak Ridge National Laboratory, Fig. 3) as well as high-resolution synchrotron X-ray diffraction (XRD) data (11-BM at Argonne National Laboratory, Fig. S1†). In both types of diffraction data, peak broadening is evident. Scanning electron microscope (SEM) images show anisotropic particles with sub-micron features in two dimensions and one longer axis in the order of microns (Fig. 4c and d). This indicates that finite size effects give rise to the reflection-dependent broadening in diffraction data.

Gruehn's reported *R*-Nb_2O_5 structure was used as a starting model for refinements of the atomic structure model against neutron and X-ray diffraction data [International Crystal Structure Database (ICSD) collection code 25765].[25] Rietveld refinement against neutron diffraction data resulted in minor changes to lattice parameters and atom positions, resulting in a fit that captures the data well (Fig. 3). Similar parameters were found from the refinement of synchrotron XRD data (Fig. S1†). Details of refinement parameters and the resulting structures are provided in Tables S1 and S2.†

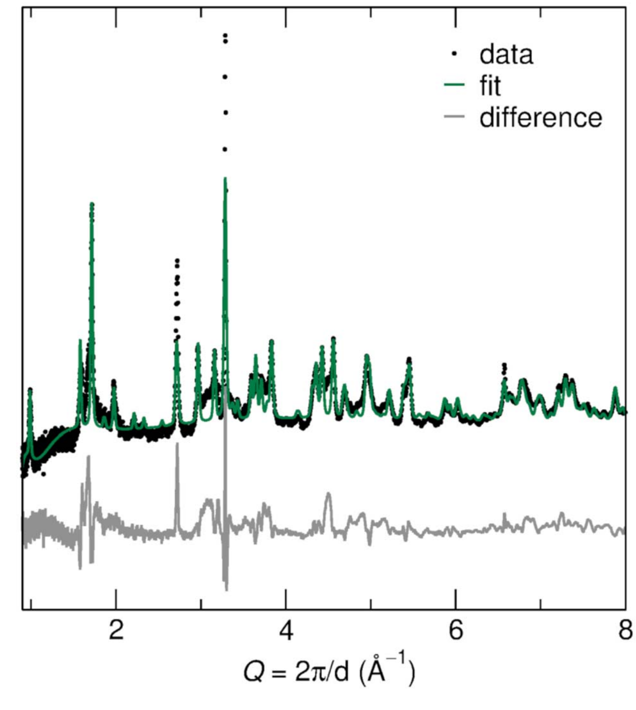

Fig. 3 Rietveld refinement against neutron diffraction data for the prepared *R*-Nb_2O_5 shows good agreement between the measured and calculated patterns. The largest differences occur in regions with diffuse scattering, as well as for two reflections that are underestimated in the calculated data. Details of the refined structure parameters are provided in the ESI.†

The differences between the measured data and calculated fit have two primary origins: diffuse scattering near Q of 1.5 Å^{-1} and 3 Å^{-1}, and peak intensity mismatch near Q of 2.9 Å^{-1} and 3.25 Å^{-1} (Fig. 3). The diffuse scattering features suggest low crystallinity, disorder, or a combination. Even after accounting for anisotropic particle shape in refinements, there is a remaining intensity mismatch for the (113), (11$\bar{3}$), and (020) reflections, which are especially narrow and accordingly must be associated with the long axis of the particles. Similar reflection-dependent broadening has also been identified for KNb_3O_8,[18] the precursor from which this *R*-Nb_2O_5 was prepared (Fig. 4a).

The elongated rectangular morphology of *R*-Nb_2O_5 comes from the morphology of the KNb_3O_8 and $H_3ONb_3O_8$ precursors (Fig. 4a and b). The layered nature of the KNb_3O_8 atomic structure drives preferential growth along specific crystallographic directions.[18] The underlying particle shape is retained through ion-exchange and low temperature heating of the prepared product. This synthetic route did not allow for the preparation of larger or more isotropic *R*-Nb_2O_5 particles, which was beyond the scope of this work, but variations of particle size and shape may be accessible from more isotropic KNb_3O_8 precursors or through alternative synthetic methods.

A notable feature of the crystal structure of *R*-Nb_2O_5 is the off-centering of Nb within the octahedra, as well as the pattern of displacements from the center between neighboring octahedra. In V_2O_5, the nearest neighbor V–O distances range from 1.58 Å to 2.8 Å, and off-centering of V^{5+} away from the center of an octahedron occurs as pairs (two displaced lower, two displaced higher, Fig. 1d).[32] In *R*-Nb_2O_5, Nb is also off-centered in the octahedra, but with a narrower distribution of Nb–O distances, ranging from 1.7 Å to 2.3 Å. In addition, off-centering occurs in a zig-zag pattern, alternating up and down for each octahedron, along the *c* direction (Fig. 2a).

2.2 Battery cycling behavior

R-Nb_2O_5 was cycled against Li metal in coin cells at various rates. At a relatively slow cycling rate of C/20 (based on the reaction of 2 mol Li per mol Nb_2O_5 in 20 h), galvanostatic cycling shows a plateau at ≈ 1.8 V for $0 \leq x \leq 1$, and a sloping region at low potentials (Fig. 5a), suggestive of two-phase and solid solution lithiation mechanisms at high and low potentials, respectively. The plateau for *R*-Nb_2O_5 is slightly higher than that for *H*-Nb_2O_5, which is at ≈ 1.6 V.[20] Over the first ≈55 cycles, unoptimized coin cells show gradual capacity fade (Fig. 5a).

Between the first and second discharge of *R*-Nb_2O_5, there are minor differences in the cycling profiles. Specifically, there is additional capacity before the plateau in the first discharge compared to later discharges. This difference is likely related to the irreversible capacity over the first cycle, with ≈0.3 mol Li per mol Nb_2O_5 remaining at the end of the first charge. This type of slight irreversibility is common in WR and related materials,[18] and has been previously attributed to sluggish diffusion of Li^+ from specific sites within WR-type structures, as well as an electronic transition from an initially electronic

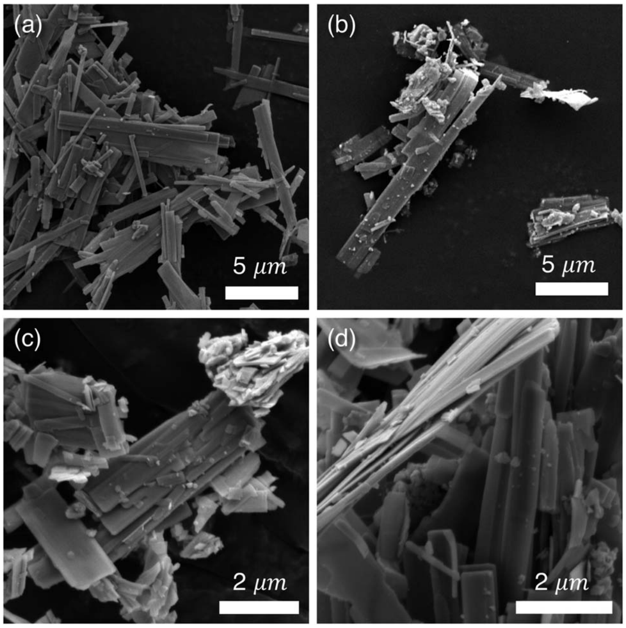

Fig. 4 SEM images of (a) precursor KNb_3O_8, (b) intermediate product of ion-exchange, $H_3ONb_3O_8$, and (c, d) R-Nb_2O_5. The elongated, rectangular particles of R-Nb_2O_5 result from its precursors. The anisotropic particle size has crystallographic origins and results in the reflection-character-dependent broadening in the diffraction data (Fig. 3).

insulator to having delocalized electron states upon slight Nb reduction.[10,11,17] Additionally, the differential capacity plot highlights minor differences in the shape of the first discharge curve relative to that of later cycles (Fig. 5). Even so, discharge and charge curves are generally symmetric, indicating similar reaction pathways on discharge and charge. This is evident in the positions of plateaus and sloped regions in galvanostatic cycling (Fig. 5a), and the corresponding peaks and diffuse features in the differential capacity plot (Fig. 5b). The symmetric cycling processes on discharge and charge are in contrast to those of the 'parent' compounds of R-Nb_2O_5, ReO_3 and V_2O_5, in which extensive and irreversible atomic structure changes during the first lithiation result in significant differences in the profile shape of the first discharge and following cycles.[29,30,35]

At faster cycling rates, electrochemical curves show good reversibility and similar electrochemical features to those after cycling at slower rates, as well as lower capacities and higher overpotentials. Changes in cycling features with increasing rate are evident in Fig. 6a, which shows the second cycle at each rate from variable rate galvanostatic cycling. The increased overpotential and more sloped nature of the cycling curves with increasing rate are highlighted in the differential capacity plot (Fig. 6b). R-Nb_2O_5 has excellent reversibility and good capacity retention, visible in cycling at C/10 and 1C in the ESI† (Fig. S3 and S4).

The decrease in capacity with increasing rate is more significant for R-Nb_2O_5 than for typical block Wadsley–Roth materials. The reversible capacity of ≈ 150 mA h g^{-1} at C/20 reduces to about 50 mA h g^{-1} at 5C (Fig. 6c), whereas typical WR block materials, *e.g.*, $TiNb_2O_7$ and PNb_9O_{25}, maintain more capacity with proportional increases in cycling rates.[11,40] While the capacities and rate capabilities of R-Nb_2O_5 do not meet those of typical WR block materials, they do exceed the reversibility and capacity retention of other related materials, such as ReO_3,[4,35] and even 'slab' material Nb_3O_7F.[15]

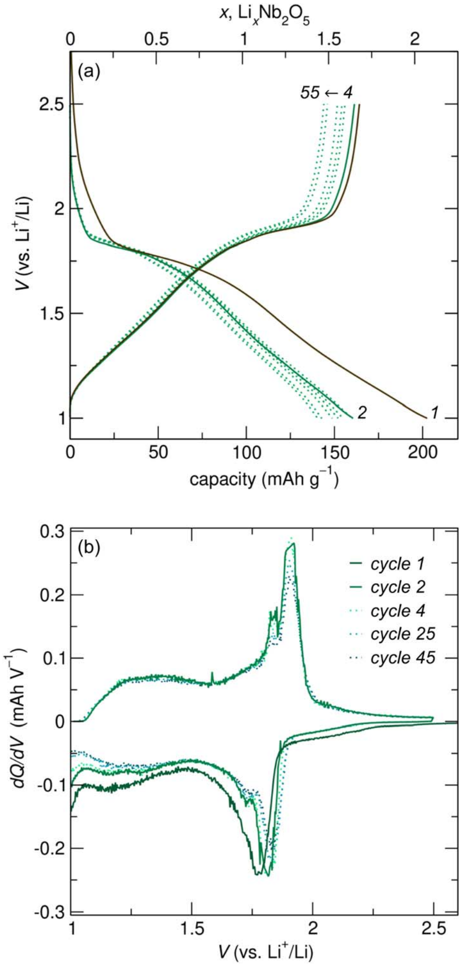

Fig. 5 (a) Galvanostatic cycling for coin cells cycled against Li metal at a rate of C/20. (a) A combination of plateaus and slopes in cycling profiles indicates two-phase and solid solution lithiation mechanisms, (b) exhibited as peaks and diffuse features in the differential capacity plot. Both plots indicate the symmetry of discharge and charge features, and their stability with cycling. In (a), the first and second cycles are represented with solid lines, and every tenth cycle following is represented by dashed lines, as numbered.

Considering that R-Nb_2O_5 has an 'idealized' V_2O_5 structure, there is a significant difference between their electrochemical behaviors during lithiation. The asymmetry observed in the charge and discharge profiles for α-V_2O_5 during lithiation, due to phase transformations into ε-, δ-, and γ- polymorphs, is significantly different than that in the highly symmetric profiles we find for R-Nb_2O_5.[29,41] The origins of these differences are discussed further in the following section.

2.3 Structural evolution with cycling

To understand the structural stability and cycling mechanism of R-Nb_2O_5, we analyzed *ex situ* synchrotron XRD data after the

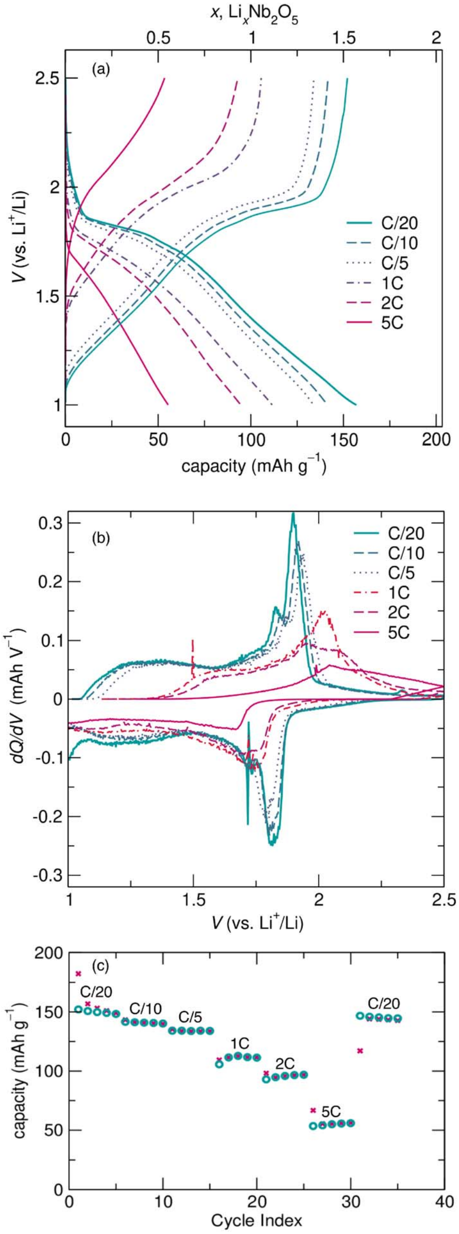

Fig. 6 (a) Galvanostatic cycling profiles and (b) differential capacity plots for coin cells cycled against Li metal at variable rates from C/20 to 5C. In (a), profiles are shown for the second cycle at each rate. (c) Capacity per cycle is shown for each rate, including the capacity recovered at C/20.

first discharge and the first charge (Fig. 7). For this, loose powder cathodes were cycled in Swagelok cells at C/20 and extracted after the first discharge (to 0.5 V, $Li_3Nb_2O_5$) and first charge (to 2.5 V, $LiNb_2O_5$). Cycling for loose powder Swagelok cells is qualitatively similar to that from coin cells (Fig. S2†). The deeper discharge relative to that of coin cells resulted in a higher first discharge capacity, but a similar reversible capacity, which suggests that the low potential capacity is associated with the formation of a solid-electrolyte interphase, storage by a conductive carbon additive, or a combination thereof.[42,43]

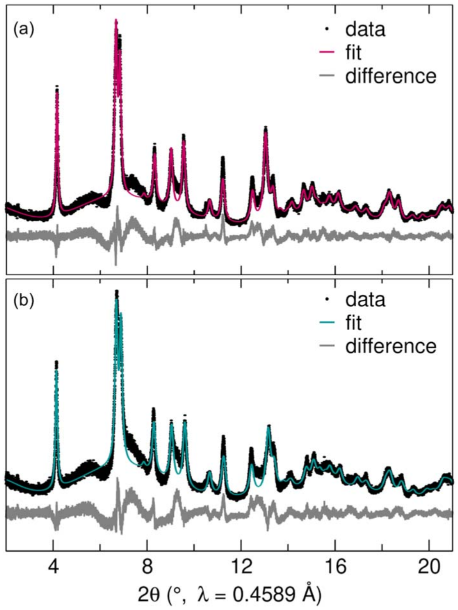

Fig. 7 Rietveld refinements of high-resolution synchrotron XRD data following (a) the first discharge and (b) the first charge of *R*-Nb_2O_5 indicate agreement between the measured and calculated patterns. Due to the poor sensitivity of X-rays to light elements, Li was excluded from the structural model and only the Nb–O framework was refined (Table 1).

Synchrotron XRD data of cycling products were used in Rietveld refinements of atomic structure models to determine the nature of these minor structural changes. For both states of charge, the *R*-Nb_2O_5 structure refined against neutron diffraction data of the prepared powder was used as the starting model. Due to the poor sensitivity of X-rays to light elements, Li was not included in the structural model, with an emphasis instead on the Nb–O framework. As in the pristine *R*-Nb_2O_5, reflection-dependant broadening was captured using isotropic crystallite size parameters, with a mix of Lorentzian and Gaussian shapes, and the preferred orientation (modeled with spherical harmonics) to account for the broadening caused by the anisotropic crystallite size. Additional information on Rietveld refinements and refined structures are provided in the ESI† (Tables S1, S2, S3, and S4).

There were no new reflections in the first discharge and charge products compared to pristine *R*-Nb_2O_5 (Fig. 3 and 7). Rather, changes in lattice parameters resulted in shifted peak positions, with the Nb–O framework retained through Li^+ intercalation and deintercalation. As in the pristine *R*-Nb_2O_5, XRD data of cycled products have diffuse scattering and broad peaks. The qualitative similarity of diffraction data for the pristine and cycled products is reflected in the quantitative results of Rietveld refinements (Table 1 and Fig. 8). Lattice parameters undergo minor contraction (a and c) and expansion (b), resulting in 4.66% and 3.56% increases in the unit cell volume (V_{uc}) of the discharge and charge products, respectively, relative to those of pristine *R*-Nb_2O_5.

Table 1 Refined unit cell parameters for pristine, discharged, and charged R-Nb_2O_5 reflect the minimal changes that result from lithiation and delithiation. In addition, changes in the size and degree of distortion of octahedra over the three states show a decrease in distortion as Nb is reduced

Composition	Pristine Nb_2O_5	Discharged $Li_3Nb_2O_5$	Charged $LiNb_2O_5$
a	3.9752(6) Å	3.94788(19) Å	3.9313(3) Å
b	3.8233(3) Å	4.04267(15) Å	4.0058(2) Å
c	12.7064(19) Å	12.6633(7) Å	12.6987(10) Å
β	90.603(13)°	90.0034(10)°	89.966(11)°
V_{uc}	193.11(4) $Å^3$	202.107(17) $Å^3$	199.98(2) $Å^3$
% Change V_{uc}[a]	—	4.66%	3.56%
Octahedral volume	10.437 $Å^3$	10.81 $Å^3$	10.6955 $Å^3$
Octahedral distortion index[b]	0.073	0.024	0.029

[a] Percent change relative to that of the pristine one. [b] Baur's distortion index (based on bond length variation)[44] calculated with VESTA.[45]

While lattice parameters are similar for pristine and cycled R-Nb_2O_5, there are notable differences in the $[NbO_6]$ octahedra for the pristine and cycled products (Fig. 8). As mentioned, Nb in R-Nb_2O_5 is less off-centered than V in V_2O_5 (Fig. 1d and f), but still has a range of Nb–O bond lengths. Baur's distortion index is a single-value quantity that can be used to describe deviations from a perfect octahedron, with 6 M–O bonds of the same length, which would have a Baur's index of 0.[44] Specifically, Baur's index represents octahedral (or tetrahedral) distortions as the deviation of bond lengths from an average bond length.[44] In the cycled products, the reduction in Baur's index reflects the decrease in Nb off-centering with the reduction of Nb^{5+} during lithiation (Fig. 8). In pristine Nb_2O_5, Nb^{5+} has an electronic configuration $[Kr]5s^24d^0$; at the *ex situ* states of charge evaluated, there is at least some reduction of Nb away from this d^0 electron configuration. The reduced oxidation state of Nb relieves the second-order Jahn-Teller distortion,[10,11,17] which is commonly active for fully oxidized early transition metals, such as Nb.[46] The reduction of Nb, and thus Nb off-centering, following discharge and charge results in nearly identical crystal structures at these states of charge (Fig. 8, Tables 1, and S1, S2, S3, and S4).

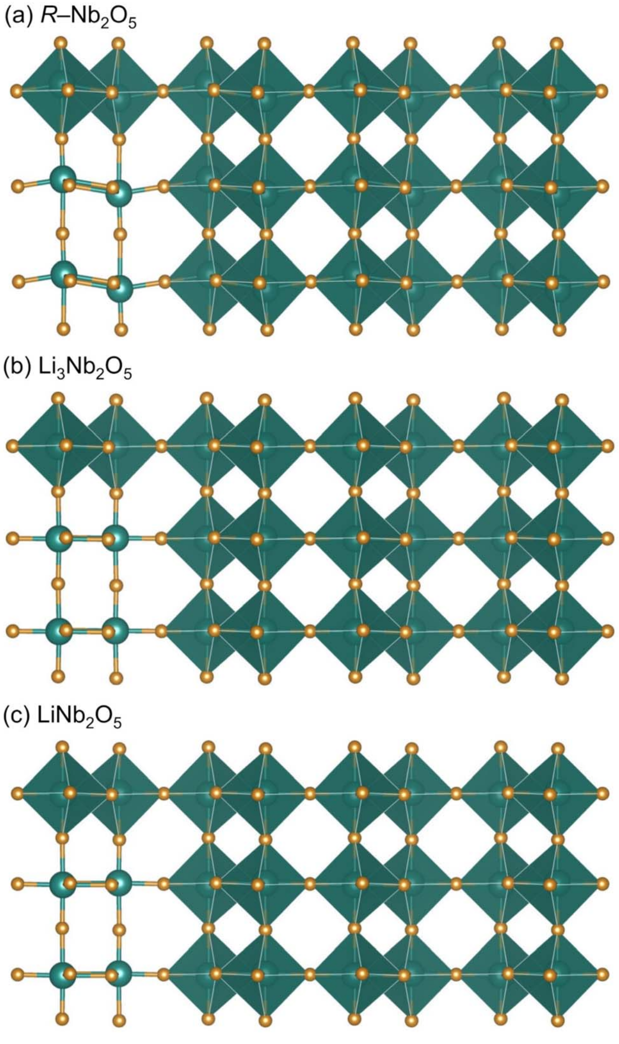

Fig. 8 Refined structures of (a) R-Nb_2O_5, and (b) lithiated product of the first discharge to 0.5 V, and (c) the following first charge to 2.5 V.

In contrast to ReO_3 and V_2O_5, R-Nb_2O_5 has minimal structure evolution during the first discharge (Fig. 8).[29,35] The difference in cycling behavior and structural stability between R-Nb_2O_5 and Nb_3O_7F is especially interesting as both have slab structures with ReO_3-like regions connected by parallel, non-intersecting crystallographic shear-planes.[27] The difference in their behavior is most likely a consequence of the difference in the width of their slabs. The extended-defect-based structures can be described as $(2 \times \infty)_\infty$ for R-Nb_2O_5, and $(3 \times \infty)_\infty$ for Nb_3O_7F.[3]

3 Conclusions

Based on our findings, R-Nb_2O_5 can serve as a 'structural bridge' between Wadsley–Roth block structures and V_2O_5 in terms of polyhedral distortions, polyhedral connectivity, and the consequences thereof for structural stability during cycling. Relative to V_2O_5, we show that bridging layers to form a three-dimensionally connected structure, as in its 'idealized' structure, stabilizes it against polyhedral rotations associated with irreversible structural changes. For WR structures, this work demonstrates for the first time that a $(2 \times \infty)_\infty$ slab structure, with only parallel (rather than intersecting) shear planes, is stable against polyhedral rotations at corner-sharing vertices during electrochemical cycling. This is in contrast to what has been found for Nb_3O_7F, in which non-intersecting crystallographic shear planes that link three-octahedron-wide slabs, denoted as $(3 \times \infty)_\infty$, do not provide structural stability during lithiation. Thus, the combination of three-dimensionally connected polyhedra and non-intersecting shear planes with a smaller slab width results in the stability of R-Nb_2O_5 against unfavorable distortions, making it a high voltage anode candidate, and moreso, a link between heavily studied material families.

In the context of published work on related structures, we illustrate how lithiation in isotypic materials induces varying degrees of structural changes and phase transformations, which have direct impacts on Li^+ diffusion pathways. The highly symmetric charge discharge profile for R-Nb_2O_5 indicates that similar sequences of phase transformations occur during lithiation and delithiation. Furthermore, the minimal structural changes result in the retention of square channels that resemble the fast Li^+ transport pathways in WR block structures. Future work to further characterize Li^+ and electronic conduction, as well as long-term cycling stability, will provide additional insights into bridge classes of early transition metal oxide electrode materials, including Wadsley–Roth block structures and V_2O_5.

4 Experimental

4.1 Synthesis

Phase pure R-Nb_2O_5 was prepared from precursors synthesized using the molten salt reaction by ion-exchange methods adapted from reported methods.[18,36,47] Precursor KNb_3O_8 was prepared by ball-milling K_2CO_3 (Sigma Aldrich, ≥ 99%), Nb_2O_5 (Sigma Aldrich, 99.99%), and KCl (Sigma Aldrich, ≥99%) in molar ratios of 1 : 3 : 12 in ethanol (Thermo Fisher, reagent grade) for 30 min. Ethanol was evaporated under ambient conditions and the resulting mixture was heated in a covered alumina crucible at 800 °C for 5 h in air, with a heating rate of $3° \text{ min}^{-1}$ and allowed to cool passively with a furnace. The reacted powder was washed with warm deionized (DI) water to remove KCl; the mixture was centrifuged and decanted to isolate KNb_3O_8 powder, which was dried in air.

The prepared KNb_3O_8, ≈1 g, was stirred in 100 mL of 7 M HNO_3 for 3 days to prepare $H_3ONb_3O_8$ *via* ion-exchange.[36] As before, the solid product was isolated and washed using DI water, centrifugation, and decanting. After drying at room temperature, $H_3ONb_3O_8$ powder was heated in air at 600 °C for 2 h, yielding R-Nb_2O_5.[36] Engineering controls (*i.e.*, ventilation hood) and personal protective equipment should always be used when handling hazardous materials, such as strong acids.

4.2 X-ray and neutron diffraction

The phase purity of the intermediates and final products was initially evaluated using Rigaku Miniflex and Panalytical X'Pert Powder diffractometers. High-resolution synchrotron XRD was carried out through mail-in from beamline 11-BM at the Advanced Photon Source at Argonne National Laboratory. Synchrotron X-rays had a calibrated wavelength of 0.4589 Å and powders were measured in transmission mode in 0.8 mm diameter Kapton capillaries sealed with epoxy at both ends.

For *ex situ* synchrotron XRD of cycled R-Nb_2O_5, powder cathodes (8 : 2 mass ratio of Nb_2O_5 and SuperP) were extracted from Swagelok half-cells cycled to a specified state of charge. The powders were washed with dimethyl carbonate (DMC), dried under vacuum, and ground with an agate mortar and pestle in an Ar-filled glove box. The samples were sealed under Ar in secondary containment for shipping and removed just prior to measurements to minimize exposure to moisture.

Neutron diffraction data of the as-prepared R-Nb_2O_5 were collected using a POWGEN diffractometer at the Spallation Neutron Source (SNS) at Oak Ridge National Laboratory (ORNL) through the mail-in program. The powders were loaded into a 6 mm diameter vanadium can. Data were collected in time-of-flight for 2 h with a center wavelength of 1.5 Å.

Structural data were refined using GSAS-II[48] and Topas Academic v7.[49] VESTA was used to visualize the crystal structures and for quantitative descriptions of $[NbO_6]$ octahedra.[45]

4.3 Electron microscopy

Scanning electron microscopy (SEM) was carried out using a TESCAN MIRA3 microscope with a beam voltage of 8 keV and a working distance of 15 mm. The samples were prepared on carbon tape and sputtered with a thin layer of gold to prevent charging.

4.4 Battery assembly and electrochemical studies

R-Nb_2O_5 was cycled in half-cell batteries with a Li metal anode (MTI, 99.9%). For preliminary cycling and *ex situ* synchrotron XRD, loose powder cathodes (Nb_2O_5 and SuperP in 8 : 2 mass ratio, mixed in an agate mortar and pestle) were assembled in Swagelok cells. For coin cells, cast cathode films were prepared by mixing R-Nb_2O_5 with Ketjen Black (MSE Supplies) and polyvinylidene floride (PVDF) in a 7.5 : 1.5 : 1 mass ratio, respectively; *N*-methyl-2-pyrollidone was used as a solvent for PVDF during casting on copper foil (MSE Supplies) using a 15 μm doctor blade.

For both cell configurations, the electrolyte was 1 M $LiPF_6$ in a mixture (1 : 1 by volume) of ethylene carbonate and DMC. For Swagelok cells, the cathode and anode were separated by two Whatman glass filter dryer (GFD) disks; for coin cells, the separator was polypropylene (Celgard 2500, 25 μm). The cells were assembled in an Ar-filled glovebox. Swagelok cells were cycled galvanostatically at various rates in terms of C, such that C is based on the reaction of 2 mol of Li. Coin cells were cycled galvanostatically at rates of C/20, C/10 and 1C with an upper potential limit of 2.5 V and a lower potential limit of 1 V. Additionally, cells were cycled with varying cycling rates of C/20, C/10, C/5, 1C, 2C, and 5C for 5 consecutive cycles, and a final set at C/20.

Author contributions

KP: conceptualization; data curation; formal analysis; investigation; visualization; writing – original draft, reviewing and editing. ADL: investigation; especially synthesis and initial characterization (laboratory XRD). SG: investigation; especially characterization (SEM imaging). MMB: conceptualization; formal analysis; project administration; resources; supervision; visualization; writing – original draft, reviewing and editing.

Conflicts of interest

There are no conflicts to declare.

Acknowledgements

The authors acknowledge MMB's startup support. Use of the Advanced Photon Source at Argonne Nationals Laboratory was supported by the U. S. Department of Energy (DOE), Office of Science, Office of Basic Energy Sciences, under Contract No. DE-AC02-06CH11357. Synchrotron XRD was carried out at Argonne National Laboratory at beamline 11-BM through the general user proposal mail-in program (GUP-75192). The neutron scattering portion of this research used resources at Oak Ridge National Laboratory's Spallation Neutron Source, a DOE Office of Science User Facility operated by the Oak Ridge National Laboratory (mail-in POWGEN data through IPTS-29055). This research made use of the Research Service Center at the University of Florida and the Materials Science and Engineering undergraduate research laboratory. The authors thank POWGEN staff for support with mail-in experiments, especially Dr Alicia M. Manjon Sanz. The authors also thank Dr Allyson Fry-Petit for helpful discussions about Topas and Dr Kit McColl for exciting discussions on early transition metal oxide materials. Furthermore, all authors acknowledge the broad and consistent support of all members of the Butala Research Group, especially John D. Langhout.

References

1 A. Magnéli, Structures of the ReO_3-type with Recurrent Dislocations of Atoms: 'Homologous Series' of Molybdenum and Tungsten Oxides, *Acta Crystallogr.*, 1953, **6**, 495–500.
2 S. Andersson and A. D. Wadsley, Crystallographic Shear and Diffusion Paths in Certain Higher Oxides of Niobium, Tungsten, Molybdenum and Titanium, *Nature*, 1966, **211**, 581–583.
3 L. R. Eyring and L. T. Tai, The Structural Chemistry of Extended Defects, *Annu. Rev. Phys. Chem.*, 1973, **24**, 189–206.
4 R. Cava, A. Santoro, D. W. Murphy, S. M. Zahurak and R. S. Roth, Structural Aspects of Lithium Insertion in Oxides: Li_xReO_3 and $Li_2FeV_3O_8$, *Solid State Ionics*, 1981, **5**, 323–326.
5 A. A. Voskanyan and A. Navrotsky, Shear Pleasure: The Structure, Formation, and Thermodynamics of Crystallographic Shear Phases, *Annu. Rev. Mater. Res.*, 2021, **51**, 521–540.
6 R. Kanno, Y. Kawamoto, Y. Takeda, S. Ohashi, N. Imanishi and O. Yamamoto, Carbon Fiber as a Negative Electrode in Lithium Secondary Cells, *J. Electrochem. Soc.*, 1992, **139**, 3397.
7 M. G. Verde, L. Baggetto, N. Balke, G. M. Veith, J. K. Seo, Z. Wang and Y. S. Meng, Elucidating the Phase Transformation of $Li_4Ti_5O_{12}$ Lithiation at the Nanoscale, *ACS Nano*, 2016, **10**, 4312–4321.
8 M. M. Thackeray and K. Amine, $Li_4Ti_5O_{12}$ Spinel Anodes, *Nat. Energy*, 2021, **6**, 683.
9 K. J. Griffith, A. C. Forse, J. M. Griffin and C. P. Grey, High-Rate Intercalation without Nanostructuring in Metastable Nb_2O_5 Bronze Phases, *J. Am. Chem. Soc.*, 2016, **138**, 8888–8899.
10 K. J. Griffith, K. M. Wiaderek, G. Cibin, L. E. Marbella and C. P. Grey, Niobium Tungsten Oxides for High-rate Lithium-ion Energy Storage, *Nature*, 2018, **559**, 556–563.
11 M. B. Preefer, M. Saber, Q. Wei, N. H. Bashian, J. D. Bocarsly, W. Zhang, G. Lee, J. Milam-Guerrero, E. S. Howard, R. C. Vincent, B. C. Melot, A. Van der Ven, R. Seshadri and B. S. Dunn, Multielectron Redox and Insulator-to-Metal Transition upon Lithium Insertion in the Fast-Charging, Wadsley–Roth Phase PNb_9O_{25}, *Chem. Mater.*, 2020, **32**, 4553–4563.
12 R. C. Vincent, Y. Luo, J. L. Andrews, A. Zohar, Y. Zhou, Q. Yan, E. M. Mozur, M. B. Preefer, J. N. Weker, A. K. Cheetham, J. Luo, L. Pilon, B. C. Melot, B. Dunn and R. Seshadri, High-Rate Lithium Cycling and Structure Evolution in Mo_4O_{11}, *Chem. Mater.*, 2022, **34**, 4122–4133.
13 J. Muller, J. Joubert and M. Marezio, Synthese et Structure Cristalline d'un Nouvel Oxyde Mixte "FeV_3O_8" ($Fe_xV_{1-x}O_2$; $x \simeq 0.25$), *J. Solid State Chem.*, 1979, **27**, 191–199.
14 A. R. Balakrishna, Crystallographic Design of Intercalation Materials, *J. Electrochem. Energy Convers. Storage*, 2022, **19**, 040802.
15 N. H. Bashian, M. B. Preefer, J. Milam-Guerrero, J. J. Zak, C. Sendi, S. A. Ahsan, R. C. Vincent, R. Haiges, K. A. See, R. Seshadri and B. C. Melot, Understanding the Role of Crystallographic Shear on the Electrochemical Behavior of Niobium Oxyfluorides, *J. Mater. Chem. A*, 2020, **8**, 12623–12632.
16 M. Saber, M. B. Preefer, S. K. Kolli, W. Zhang, G. Laurita, B. Dunn, R. Seshadri and A. Van der Ven, Role of Electronic Structure in Li Ordering and Chemical Strain in the Fast Charging Wadsley–Roth Phase PNb_9O_{25}, *Chem. Mater.*, 2021, **33**, 7755–7766.
17 C. P. Koçer, K. J. Griffith, C. P. Grey and A. J. Morris, Lithium Diffusion in Niobium Tungsten Oxide Shear Structures, *Chem. Mater.*, 2020, **32**, 3980–3989.
18 K. McColl, K. J. Griffith, R. L. Dally, R. Li, J. E. Douglas, K. R. Poeppelmeier, F. Corà, I. Levin and M. M. Butala, Energy Storage Mechanisms in Vacancy-ordered Wadsley–Roth Layered Niobates, *J. Mater. Chem. A*, 2021, **9**, 20006–20023.
19 H. Schäfer, R. Gruehn and F. Schulte, The Modifications of Niobium Pentoxide, *Angew. Chem., Int. Ed.*, 1966, **5**, 40–52.
20 T. Li, G. Nam, K. Liu, J.-H. Wang, B. Zhao, Y. Ding, L. Soule, M. Avdeev, Z. Luo, W. Zhang, *et al.*, A Niobium Oxide with a Shear Structure and Planar Defects for High-power

Lithium Ion Batteries, *Energy Environ. Sci.*, 2022, **15**, 254–264.

21 H. Nakayama, M. Nose, S. Nakanishi and H. Iba, Electrochemical Reactions of Layered Niobate Material as Novel Anode for Sodium Ion Batteries, *J. Power Sources*, 2015, **287**, 158–163.

22 J. W. Kim, V. Augustyn and B. Dunn, The Effect of Crystallinity on the Rapid Pseudocapacitive Response of Nb_2O_5, *Adv. Energy Mater.*, 2012, **2**, 141–148.

23 V. Augustyn, P. Simon and B. Dunn, Pseudocapacitive Oxide Materials for High-rate Electrochemical Energy Storage, *Energy Environ. Sci.*, 2014, **7**, 1597–1614.

24 A. A. Lubimtsev, P. R. Kent, B. G. Sumpter and P. Ganesh, Understanding the Origin of High-rate Intercalation Pseudocapacitance in Nb_2O_5 Crystals, *J. Mater. Chem. A*, 2013, **1**, 14951–14956.

25 R. Gruehn, Eine weitere neue Modifikation des niobpentoxids, *J. Less-Common Met.*, 1966, **11**, 119–126.

26 O. Aalling-Frederiksen, M. Juelsholt, A. S. Anker and K. M. Jensen, Formation and growth mechanism for Niobium Oxide Nanoparticles: Atomistic Insight from in-situ X-ray Total Scattering, *Nanoscale*, 2021, **13**, 8087–8097.

27 S. Andersson, On the Description of Complex Inorganic Crystal Structures, *Angew. Chem., Int. Ed. Engl.*, 1983, **22**, 69–81.

28 M. Israelsson and L. Kihlborg, The Crystal Structure of Monoclinic Wolfram Vanadium Oxide, $W_3V_5O_{20}$, an 0-D Structure Related to R-Nb_2O_5, *J. Solid State Chem.*, 1970, **1**, 469–477.

29 L. R. De Jesus, J. L. Andrews, A. Parija and S. Banerjee, Defining Diffusion Pathways in Intercalation Cathode Materials: Some Lessons from V_2O_5 on Directing Cation Traffic, *ACS Energy Lett.*, 2018, **3**, 915–931.

30 P. Schofield, Y. Luo, D. Zhang, W. Zaheer, D. Santos, G. Agbeworvi, J. D. Ponis, J. V. Handy, J. L. Andrews, E. J. Braham, *et al.*, Doping-Induced Pre-Transformation to Extend Solid-Solution Regimes in Li-Ion Batteries, *ACS Energy Lett.*, 2022, **7**, 3286–3292.

31 L. Kihlborg, Crystal Structure of $(MO_{0.3}V_{0.7})_2O_5$ of R-Nb_2O_5 type and a comparison with Structures of V_2O_5 and V_2MoO_8, *Acta Chem. Scand.*, 1967, **21**, 2495.

32 V. Shklover, T. Haibach, F. Ried, R. Nesper and P. Novak, Crystal Structure of the Product of Mg^{2+} Insertion into V_2O_5 Single Crystals, *J. Solid State Chem.*, 1996, **123**, 317–323.

33 K. Meisel, Rheniumtrioxyd. III. Mitteilung. Ueber die Kristallstruktur des Rheniumtrioxyds, *Z. Anorg. Allg. Chem.*, 1932, **207**, 121–128.

34 S. Andersson, Crystal Structure of Nb_3O_7F, *Acta Chem. Scand.*, 1964, **18**, 2339–2344.

35 N. H. Bashian, S. Zhou, M. Zuba, A. M. Ganose, J. W. Stiles, A. Ee, D. S. Ashby, D. O. Scanlon, L. F. J. Piper, B. Dunn and B. C. Melot, Correlated Polyhedral Rotations in the Absence of Polarons during Electrochemical Insertion of Lithium in ReO_3, *ACS Energy Lett.*, 2018, **3**, 2513–2519.

36 R. Nedjar, M. Borel and B. Raveau, $H_3ONb_3O_8$ and HNb_3O_8: New protonic oxides with a layer structure involving ion exchange properties, *Mater. Res. Bull.*, 1985, **20**, 1291–1296.

37 M. Gasperin, Structure du Triniobate (V) de Potassium KNb_3O_8, un Niobate Lamallaire, *Acta Crystallogr., Sect. B: Struct. Crystallogr. Cryst. Chem.*, 1982, **B38**, 2024–2026.

38 R. Nedjar, M. M. Borel, A. Leclaire and B. Raveau, The Sodium Niobate $NaNb_3O_8$: A Novel Lamellar Oxide Synthesized by Soft Chemistry, *J. Solid State Chem.*, 1987, **71**, 182–188.

39 Z. Y. Zhan, C. Y. Xu, L. Zhen, W. S. Wang and W. Z. Shao, Large-Scale Synthesis of Single-Crystalline KNb_3O_8 Nanobelts via a Simple Molten Salt Method, *Ceram. Int.*, 2010, **36**, 679–682.

40 K. J. Griffith, I. D. Seymour, M. A. Hope, M. M. Butala, L. K. Lamontagne, M. B. Preefer, C. P. Kocer, G. Henkelman, A. J. Morris, M. J. Cliffe, *et al.*, Ionic and electronic conduction in $TiNb_2O_7$, *J. Am. Chem. Soc.*, 2019, **141**, 16706–16725.

41 C. Delmas, H. Cognac-Auradou, J. Cocciantelli, M. Ménétrier and J. Doumerc, The $Li_xV_2O_5$ System: An Overview of the Structure Modifications induced by the Lithium Intercalation, *Solid State Ionics*, 1994, **69**, 257–264.

42 K. A. See, M. Lumley, G. D. Stucky, C. P. Grey and R. Seshadri, Reversible Capacity of Conductive Carbon Additives at Low Potentials: Caveats for Testing Alternative Anode Materials for Li-Ion Batteries, *J. Electrochem. Soc.*, 2017, **164**, A327–A333.

43 M. M. Butala, K. R. Danks, M. A. Lumley, S. Zhou, B. C. Melot and R. Seshadri, MnO Conversion in Li-Ion Batteries: *In Situ* Studies and the Role of Mesostructuring, *ACS Appl. Mater. Interfaces*, 2016, **8**, 6496–6503.

44 W. H. Baur, The Geometry of Polyhedral Distortions. Predictive Relationships for the Phosphate Group, *Acta Crystallogr., Sect. B: Struct. Crystallogr. Cryst. Chem.*, 1974, **30**, 1195–1215.

45 K. Momma and F. Izumi, VESTA3 for Three-dimensional Visualization of Crystal, Volumetric and Morphology Data, *J. Appl. Crystallogr.*, 2011, **44**, 1272–1276.

46 P. S. Halasyamani, Asymmetric Cation Coordination in Oxide Materials: Influence of Lone-Pair Cations on the Intra-octahedral Distortion in d^0 Transition Metals, *Chem. Mater.*, 2004, **16**, 3586–3592.

47 L. Li, J. Deng, R. Yu, J. Chen, X. Wang and X. Xing, Phase Evolution in Low-dimensional Niobium Oxide Synthesized by a Topochemical Method, *Inorg. chem.*, 2010, **49**, 1397–1403.

48 B. H. Toby and R. B. Von Dreele, GSAS-II: the Genesis of a Modern Open-source All Purpose Crystallography Software Package, *J. Appl. Crystallogr.*, 2013, **46**, 544–549.

49 A. A. Coelho, TOPAS and TOPAS-Academic: An Optimization Program Integrating Computer Algebra and Crystallographic Objects Written in C++, *J. Appl. Crystallogr.*, 2018, **51**, 210–218.